IEEE Access
Multidisciplinary | Rapid Review | Open Access Journal

Received February 1, 2019, accepted February 26, 2019, date of publication March 5, 2019, date of current version March 25, 2019.

Digital Object Identifier 10.1109/ACCESS.2019.2902854

Matching Corresponding Regions of Interest on Cranio-Caudal and Medio-Lateral Oblique View Mammograms

XIAOMAN DUAN[1], GENGGENG QIN[1,2], QINGQING LING[1], SINA WANG[2], ZEYUAN XU[2], HUI ZENG[2], BIN LI[1], WEIGUO CHEN[2], LINGHONG ZHOU[1], AND YUAN XU[1]

[1]School of Biomedical Engineering, Southern Medical University, Guangzhou 510515, China
[2]Department of Radiology, Nanfang Hospital, Southern Medical University, Guangzhou 510515, China

Corresponding authors: Linghong Zhou (smart@smu.edu.cn) and Yuan Xu (yuanxu@smu.edu.cn)

This work was supported in part by the Chinese National Key R&D Development Program under Grant 2016YFA0202003, in part by the National Natural Science Foundation of China under Grant 81601493 and Grant 81571771, in part by the Guangdong Natural Science Foundation of China under Grant 2016A030310388, Grant 2017A030313692, and Grant 2018A0303130215, in part by the Science and Technology Planning Project of Guangdong under Grant 2015B020233008 and Grant 2015B020233002, and in part by the Guangzhou Science and Technology Project under Grant 201604020058.

ABSTRACT Automatically matching corresponding regions of interest (ROIs) on two-view images is valuable in breast cancer diagnosis, benefiting of saving time and cutting the workload. We propose a method for matching the corresponding ROIs by integrating the geometric model and image similarity searching. The geometric model is implemented by restoring a free breast in the 3D space from two-view preprocessed breast contours. Then, the possible position of the ROI center on cranio-caudal (CC)/medio-lateral oblique (MLO) view image is represented by three feature points in the 3D space. As the view changes, these points can be mapped onto the MLO/CC view image. A matching strip is created later according to the confidence interval, within which the specific position of the ROI can be located by image similarity searching. The experiments were conducted on 273 pairs of mammograms with 400 calcifications and 284 pairs with 300 masses to verify the accuracy of the geometric model and similarity searching. The mean absolute error between the curves and the ROI centers was 3.36 ± 2.90 mm. For 95% detection sensitivity, the confidence interval was ± 8.77 mm. For calcifications, the mean distance between the centers of the matched ROIs and the reference was 3.92 ± 4.61 mm. About 93.46% cases had overlap greater than 50%, and 92.46% cases had overlap greater than 75%. For masses, the mean distance was 6.15 ± 7.08 mm. About 88.46% cases had overlap greater than 50%, and 85.58% cases had overlap greater than 75%.

INDEX TERMS Mammogram, geometric model, matching ROIs, similarity measure.

I. INTRODUCTION

Some lesions cannot be easily observed in single mammogram for some cases due to superimposition of breast parenchymal patterns/tissues [1], [2]. When reading mammograms, breast radiologists are often confused by some regions of interest (ROIs), doubting they are real lesions or false positives [3]. To solve this problem, modern mammography routinely acquire two-view images (cranio-caudal (CC) and medio-lateral oblique (MLO)) [4], [5] for more information from different perspectives. It requires radiologists to observe the two-view images and compare the image information to ensure that what they observe are the same ROIs, despite high accuracy but poor efficiency. Automatically matching the same ROIs on two-view images is valuable for radiologists in breast cancer diagnosis, benefiting of saving time and cutting the workload. This is a very important issue with which breast radiologists deal every day.

To our knowledge, there have been a few techniques aimed to match corresponding positions between CC and MLO view images [6]–[19]. Such techniques have been mainly classified as geometry-based method [20]–[23], similarity measurement method [9], [24], [25], and classifier-based method [3], [4], [15], [26]–[28]. Geometry-based method can

The associate editor coordinating the review of this manuscript and approving it for publication was Sudipta Roy.

be further divided into plane-based and space-based method. Plane-based method mainly establishes the correspondence through distances between ROI centers and nipples. The distances from ROI centers to nipples on CC images are approximately equal to the distances on MLO images from the corresponding ROI centers to the nipples. Thus, an arc is acquired, indicating the corresponding position relationship on two-view images (hereafter termed Arc method) [6], [7], [17]. Another method utilizes inclined lines as registrations that are paralleling to chests. The inclined distances from the ROI centers to nipples on MLO images can be approximately regarded as the horizontal distances from the corresponding ROI centers to the nipples on CC images (hereafter termed Line method) [8], [9], [11]. Unexpected and unsatisfactory results may be produced sometimes because only distance constraint is applied. For space-based method, Kita *et al*. [21] proposed a geometric model that simulated deformation and calculated an epipolar curve on second view images. This method could predict the location with mean absolute error (MAE) of 6.78mm for 37 lesions. Yam *et al*. [22] used geometric constraint and matching criterion to developed a method, with MAE of 6.5mm for 35 lesions. In terms of similarity measurement method, a principle widely adopted is that high similarity is shown between same lesions on CC and MLO images compared with mismatched lesions. Yang *et al.* [27] utilized three features (gradient code, energy code, and local entropy code) to match the specific region position by a binary decision tree (BDT). For classifier-based method, it is usually based on a cascade of classifiers that aim to eliminate an increasingly larger number of false positives while keeping a large proportion of the true positives [4]. Van and Timp [29] proposed a method to link candidate regions determined by single-view CAD scheme in MLO and CC projections by using linear discriminate analysis (LDA). The effectiveness of the method was tested and verified by 412 cancer cases, and accuracy of 82% was obtained. However, each approach has its own limitations. First, geometry-based method mainly obtains registering lines or curves rather than specific positions of ROIs, which is usually used as auxiliary to finalize specific locations. Furthermore, set-up errors in mammography make the registering results oscillate near the real positions. Second, despite relatively high similarity between CC and MLO images for most lesions, using similarity measurements in large search area can easily increase the false positive proportion. Third, most of current classifier-based method is only sensitive to one specific lesion, either the calcification or mass. However, there are usually multiple types of ROIs on an image at the same time which radiologists want to identify to ensure they are real lesions or false positives.

In this paper, we propose a method for matching any corresponding ROIs by integrating geometric model and similarity searching (GM-SS). The geometric model is implemented by restoring a free breast in 3D space from two-view preprocessed breast contours. Then the possible position of the ROI center on CC/MLO view image is represented by three feature points in 3D space. As the view changing, these points can be mapped onto MLO/CC view image. A matching strip is created later according to confidence interval, within which the specific position of the ROI can be located via image similarity searching. Compared with the existing methods, GM-SS has some great advantages. Specifically, GM-SS can obtain specific positions on second images. More importantly, GM-SS is capable of matching any kinds of ROIs because it can always obtain corresponding matching strips of ROIs via the geometric model. In addition, this technique has high practicability and flexibility. The only thing radiologists need to do is click on one ROI in CC/MLO image. This method will prompt the location of the same ROI in the other image. The whole process takes only 2-3 seconds.

The remainder of the paper is organized as follows. Section II describes the workflow of GM-SS and explains its specific implementation. The end of the section introduces data sets and evaluation methods. Section III presents the experimental results. Section IV discusses few related issues. Section V provides the conclusions.

II. MATERIALS AND METHODS

A. WORKFLOW

For simple instructions, we assume that the known ROI center is located on the CC image and match its corresponding ROI on the MLO image. Fig. 1 illustrates the workflow of the proposed method, which includes eight steps. In step 1, a free breast with no compression can be restored in 3D space from breast contours extracted from two-view images. In step 2, for simplification, three feature points will be selected to present the position of the ROI center in 3D space when the breast is free. In step 3, the 3D breast is rotated to simulate the direction change from CC to MLO. In step 4, compression will be implemented upon the rotated breast in MLO considering that the breast is imaged under pressure in practice. In step 5, the three featured points are mapped onto the MLO image based on X-ray projection principle. In step 6, the feature points can be continued by quadratic interpolation to obtain a continuous curve. In step 7, a matching strip is created according to confidence interval, and it is centered with the curve. In step 8, the corresponding ROI can be located on the MLO image through searching in strips by image similarity measure. The involved steps are presented in detail in the following sections.

B. IMPLEMENTATION OF THE METHOD

1) RESTORATION OF 3D BREAST

Preprocessing operations for restoration consist of contour extraction, chest line detection [30]–[32], and MLO contour rotation and extension, as shown in Fig. 2. In general, 3D objects can be easily recovered from two orthogonal projections based on stereo vision. However, the angle difference between CC and MLO views is about 40°-60° in practice. In this study, the MLO contour can be regarded as the mediolateral (ML) contour after rotation and extension operations.

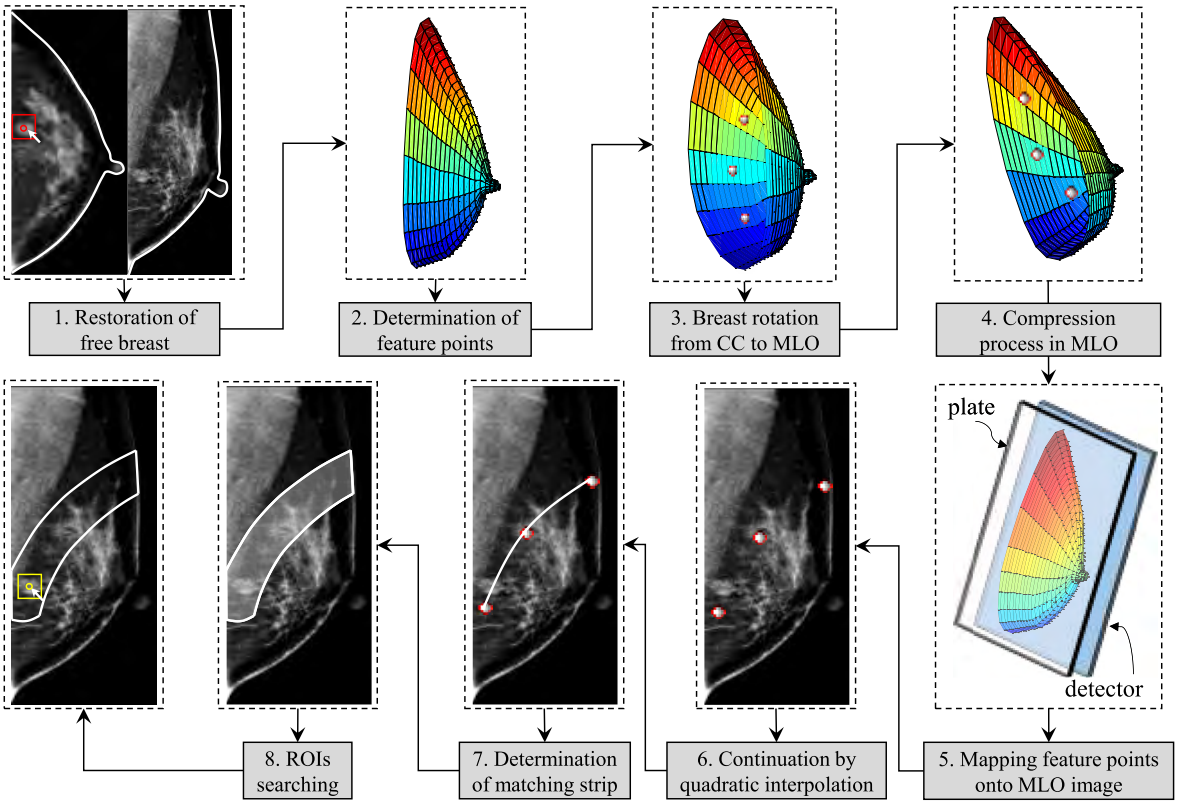

FIGURE 1. Workflow of GM-SS method.

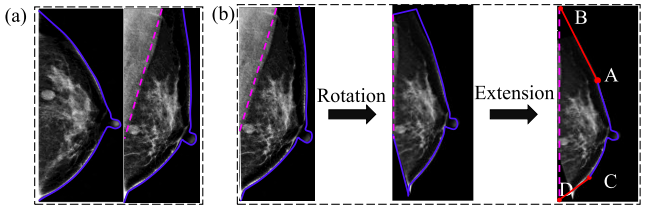

FIGURE 2. Preprocessing operations for breast restoration. (a) Contour extraction and chest line detection. (b) MLO contour rotation and extension.

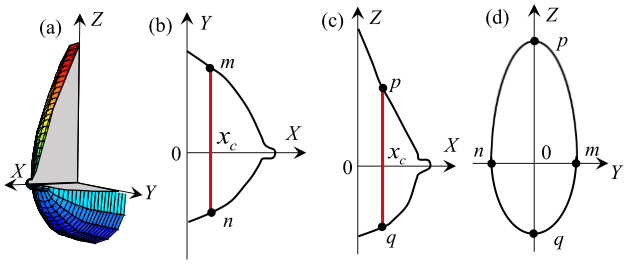

FIGURE 3. Diagram of 3D breast restoration from CC and ML contours. (a) Coordinate system for a free breast in 3D space. (b) Intersection points m and n between perpendicular $x = x_c$ and CC contour. (c) Intersection points p and q between perpendicular $x = x_c$ and ML contour. (d) Cross-section $x = x_c$ consists of the upper semi-ellipse mpn and the lower semi-ellipse mqn.

The nipple on the MLO image is regarded as the center of rotation. In addition, the contour near the chest wall is replaced by the extension of the tangent of inflection points to acquire the standardized ML contour. As shown in Fig. 2(b), A and C are the upper and lower inflection points of the MLO contour, and B and D are the corresponding intersection points between the chest wall and tangent lines. In this way, we can obtain the projections of the breast contour in two orthogonal directions (CC in vertical and ML in horizontal direction). The preprocessing operations can be automatically accomplished in this study.

Before restoration, a unified 3D coordinate system in Fig. 3(a) is introduced for convenient description. The coordinate origin is defined to be the foot of the perpendicular line from the chest to the nipple. The perpendicular line is regarded as x-axis, and z-axis lies along the chest wall with contrary direction to gravity. Then, y-axis could be determined based on the right-handed coordinate frame.

For each perpendicular $x = x_c$ in Fig. 3 (b) and (c), two intersection points, namely, m and n, with the CC contour and two intersection points, namely, p and q, with ML contour can be obtained. In this method, for each cross-section $x = x_c$, four vertex positions are acquired, as shown in Fig. 3 (d). The contour of the cross-section can be simplified with the upper semi-ellipse determined by the points of m, p, and n, and that of the lower semi-ellipse with the points of m, q, and n.

2) CALCULATION OF FEATURE POINTS

This step aims to calculate three feature points to present the 3D position of the ROI center when the breast is free. Fig. 4(a) depicts a ROI center P_l^C on the CC image. Fig. 4(b) displays a breast under compression. P_u^C, P_c^C, and P_l^C are intersection

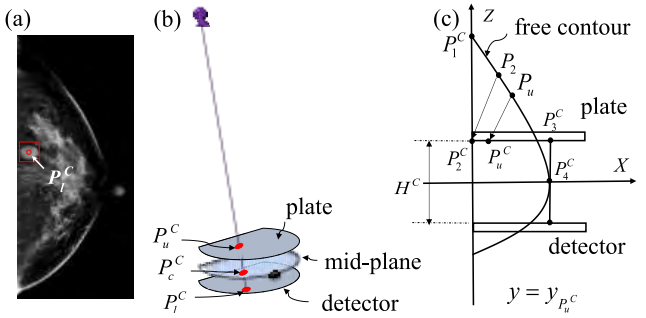

FIGURE 4. Calculation of three feature points. (a) CC image with a ROI center P_l^C. (b) Three intersection points of P_u^C, P_c^C, and P_l^C when X-ray successively passes through the compression plate, the mid-plane between the compression plate and detector, and the detector. (c) Conversion process from P_u^C into P_u.

points when X-ray successively passes through the compression plate, the mid-plane between the compression plate and the detector, and the detector. According to X-ray projection principle, both of P_u^C and P_c^C are imaged at P_l^C. Fig. 4 (c) shows the conversion process from the compression state to free. P_u, P_c, and P_l present the corresponding points of P_u^C, P_c^C and P_l^C when the breast is free. Black curve represents the free contour of the cross-section $y = y_{P_u^C}$. According to experiment results in [20], cross-section deforms only in its plane approximately, and points on the middle plane approximately remain in fixed positions during compression. Thus, the upper free contour can be simplified by the polyline of $P_1^C P_2^C P_3^C P_4^C$ after compression. P_1^C is the intersection point between the free contour and z-axis, P_2^C is the intersection point between the compression plate and z-axis, and P_2 is its corresponding point on free contour, P_3^C is the point on the compression plate with equal x-coordinate to the nipple, and P_4^C is the point of nipple, which keeps same coordinate during compression based on previous approximation. H^C is the breast thickness under CC compression. In this study, the length of the polyline of $P_2^C P_3^C P_4^C$ is supposed to be a constant during compression. In other words, the curve of $P_1^C P_2$ will be stretched to be the line of $P_1^C P_2^C$ after compression. P_u could be calculated following an equivalent relation between the curve of $P_u P_4^C$ and the polyline of $P_u^C P_3^C P_4^C$. P_l can be calculated in the same way but using the lower free contour. The position of P_c is the same as that of P_c^C because it is located on the middle plane. Thus, three feature points are acquired to present the position of the ROI center in 3D space when the breast is free. This step can be termed as decompression.

3) BREAST ROTATION AND COMPRESSION

In mammography, the X-ray source will rotate by 40°–60° from the CC view to the MLO view. The same effects can be accomplished by rotating the 3D breast by $-40°$– $-60°$ around the x-axis. Such rotation can be written as:

$$\begin{bmatrix} x' \\ y' \\ z' \end{bmatrix} = \begin{bmatrix} x \\ y \\ z \end{bmatrix} \begin{bmatrix} 1 & 0 & 0 \\ 0 & \cos\theta & \sin\theta \\ 0 & -\sin\theta & \cos\theta \end{bmatrix} \quad (1)$$

where (x, y, z) denotes the breast coordinate before rotation, and (x', y', z') is the result after rotation. θ represents the angle change between CC and MLO views. P'_u, P'_c, and P'_l represent the points of P_u, P_c, and P_l after rotation, respectively.

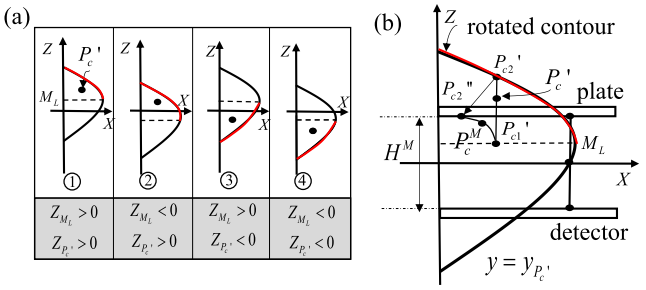

FIGURE 5. (a) Four different position relations between P'_c and its cross-section. (b) Transformation from P'_c to P_c^M. H^M is the breast thickness under compression in MLO view.

According to the real situation, the compressed positions in MLO should be acquired before mapping three feature points onto the MLO image. Considering that deformation only occurs in its own cross-section, the point after compression can be calculated through its free cross-section. For points of P'_u and P'_l, which are located on the surface of the breast skin, their corresponding points of P_u^M and P_l^M under compression in MLO can be calculated inversely by using the method described in II.B.2). For the point of P'_c inside the breast, its corresponding point P_c^M under compression is calculated using another method. Fig. 5 (a) shows four different position relations between P'_c and its cross-section of $y = y_{P'_c}$. The black dot represents the point of P'_c. M_L denotes the mid-line of the cross-section, which passes through the point of the maximum x-coordinate of the contour. $z_{P'_c}$ and z_{M_L} are the z-coordinate of P'_c and M_L. Breast contour in red are the parts involved in calculation for P_c^M. Fig. 5 (b) describes the specific transformation process from P'_c to P_c^M, which takes the first kind of position relation as an example. If we make a straight line parallel to the z-axis through P'_c, then the straight line will intersect the M_L at P'_{c1} and intersect the upper contour at P'_{c2}. P''_{c2} is the compressed point of P'_{c2} and it can be calculated inversely by using the method described in II.B.2). P'_{c1} will remain at the same position after compression. The curve of $P'_{c1} P''_{c2}$ can be represented approximately by a quadratic curve. Then the point of P_c^M will be determined based on the approximation that a curve within the breast tissue stretches uniformly during compression. The three other cases of different relative position relations could be solved using the same method. In such way, P_u^M, P_l^M, and P_c^M can be obtained.

4) DETERMINATION OF MATCHING STRIP FROM FEATURE POINTS

This section describes the procedure from three feature points under compression in MLO view to the matching strip. P_u^M, P_l^M, and P_c^M can be mapped onto the MLO image according to the X-ray projection principle. However, a possible path on the MLO image should be a continuous curve, which

indicates the possible position of the ROI center. In this study, the curve is obtained through interpolation by quadratic equations among the three feature points.

Through the preceding steps, we obtain the possible positions of the ROI centers; nevertheless, in the actual application, radiologists prefer to obtain specific ROI positions rather than a curve. Therefore, finding the specific location based on the curve is meaningful. In this study, a matching strip is created for matching specific ROI positions according to the confidence interval of 95% detection sensitivity. Additional details could be found in the Results section.

5) RECOGNITION OF SPECIFIC POSITION OF ROIS

This step aims to find the specific position of ROIs in matching strips by maximizing similarity measures. This paper proposes an integrated similarity measure called *ISM*, which can locate specific locations suitably. *ISM* is defined as:

$$ISM = e^{(-\alpha \cdot \frac{(\mu^{CC} - \mu^{MLO})^2}{2} + \beta \cdot s)} \tag{2}$$

where μ^{CC} and μ^{MLO} are the normalized gray mean of ROIs on the CC and MLO images, respectively. s denotes the coefficient of the normalized mutual information (*NMI*) [33], which is utilized to represent the similarity between two variables. The definition of s is, (3) as shown at the bottom of this page, where $p(\cdot)$ denotes probability, and $p(\cdot, \cdot)$ denotes joint probability. $I^{CC}(i, j)$ and $I^{MLO}(i, j)$ are the gray values of (i, j) in ROIs on the CC and MLO images, respectively. Larger s means higher similarity between two variables. α and β are tunable parameters that represent the weight of the two weighted terms. In this work, α and β were fixed based on the accuracy of similarity searching. Specifically, we try to optimize these parameters to obtain the minimum mean distance between the centers of the matched ROIs and the reference, which can be expressed as the following equation:

$$(\alpha, \beta) = \arg\min \left\{ \sum_{i=1}^{Q} \sum_{j=1}^{P} (u_{ij} - \overline{u}_{ij})^2 + (v_{ij} - \overline{v}_{ij})^2 \right\} \tag{4}$$

where u_{ij} and v_{ij} denote the row and column coordinates of the centers of the matched ROIs, and $\overline{u}_{ij}$ and $\overline{v}_{ij}$ represent the row and column coordinates of the reference centers, which have been identified by radiologists. P is the number of cases on per pair of images, and Q represents the total number of image pairs. This is a nonlinear minimization problem, which can be solved with the Levenberg-Marquardt Algorithm as implemented in *Minpack* [34]. On account of large difference between the mass and calcification on the image, we divided this optimization process into mass task and calcification task, independently. The optimization results in our work showed that for calcifications when α and β are 2 and 0.6, the mean distance is smallest. For masses, when α and β are 0.8 and 1, the mean distance is smallest.

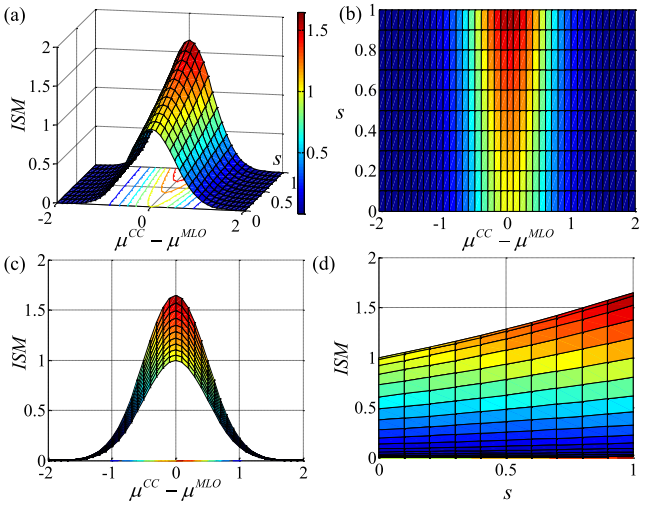

FIGURE 6. (a) 3D surface map of *ISM*, (b)-(d) corresponding top, front, and side views of the surface map, respectively.

Fig. 6 (a) displays the 3D surface map of *ISM*, which integrates μ^{CC} and μ^{MLO} into a variable for visualization. μ^{CC}-μ^{MLO} changes from -2 to 2, and s changes from 0 to 1 because μ^{CC}, μ^{MLO}, and s are all normalized values. (b) - (d) are the corresponding top, front, and side views of (a). *ISM* will be large only when μ^{CC} is approximately equal to μ^{MLO}. On this basis, *ISM* further enlarges with s increasing. In addition, when μ^{CC}-μ^{MLO} belongs to $(-0.5, 0.5)$, *ISM* is large as long as s is close to 1. In summary, *ISM* can firstly select candidate areas with similar normalized gray of ROIs in matching strips. The image information correlations between these areas and ROIs are compared thereafter to finalize the optimal matching.

TABLE 1. Distribution of data sets used in experiments.

	No. patients	No. cases	No. benign	Average size
Calcification	273	400	400	1.51mm
Mass	284	300	186	15.23mm

C. DATA SETS AND EVALUATION METHODS

Table 1 displays the distribution of data sets used in the experiment, including the number of patients (No. patients), the number of total cases (No. cases), the number of benign

$$s = \frac{\sum\limits_{I^{CC}(i,j)} p(I^{CC}(i,j)) \log(p(I^{CC}(i,j))) + \sum\limits_{I^{MLO}(i,j)} p(I^{MLO}(i,j)) \log(p(I^{MLO}(i,j)))}{\sum\limits_{I^{CC}(i,j), I^{MLO}(i,j)} p(I^{CC}(i,j), I^{MLO}(i,j)) \cdot \log(p(I^{CC}(i,j), I^{MLO}(i,j)))} \tag{3}$$

cases (NO. benign), and the average size. Note that all calcifications selected are benign because most of the malignant calcifications are widely distributed clusters. In general, these clusters are very easy to match during the diagnosis process. Therefore, in our work, benign calcification is the matched object. Mass data were randomly selected so that no homogeneous characteristics were constructed. Among the 300 masses, 186 were benign and 114 were malignant. In addition, the sizes of calcifications, the sizes and density ratings of the masses were given by radiologists, as shown in Fig. 7. The size was defined as the longest dimension. The average sizes of the calcifications and masses were 1.51mm and 15.23mm, respectively.

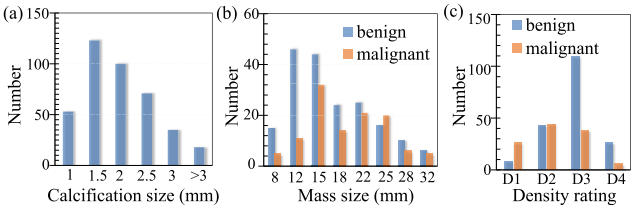

FIGURE 7. (a) Distribution of the size of calcifications. (b) Distribution of the size of benign and malignant masses. (c) Distribution of masses density ratings.

Density ratings were classified according to the Breast Imaging Reporting and Data System [35] (BI-RADS, edition 2013): D1 for entirely fatty breast, D2 for scattered fibroglandular tissue, D3 for heterogeneously dense breast, and D4 for extremely dense breast. The centers of the calcifications and masses were identified and marked on two-view images by radiologists, expressed by P_l^C on the CC image and P_l^M on the MLO image, respectively.

Data acquisition was performed in 2D digital mammography mode by using a digital breast tomosynthesis system of commercial Hologic Selenia Dimensions (Hologic Inc, USA). The tube voltage ranged from 25 kV to 32 kV. All mammograms were acquired in modern automatic exposure control (AEC) mode at 40–60 mAs. These images were processed with Hologic Selenia conventional and C-View software to improve resolution and contrast to noise ratio. The detector was readout in 1×1 binning mode with a pixel size of $70\mu\text{m} \times 70\mu\text{m}$ and image size of 3328×2560. Parameters such as distance from the X-ray source to the detector, thickness under compression in CC and MLO and angle change from CC to MLO view could be acquired from the DICOM (Digital Imaging and Communications in Medicine) files for each pair of images.

Experiments included evaluation of the accuracy of geometric model result, the accuracy of geometric model, similarity searching, and result comparisons with related works. In evaluation of geometric model, calcification images were utilized to verify the accuracy of corresponding curves. Both calcification and mass images were presented to verify the matching accuracy of similarity searching. Although in actual diagnosis, ROIs may be architectural distortions or asymmetries (asymmetry, global asymmetry, focal asymmetry, and developing asymmetry) [36]. The characteristics of them are not significant on images and the morphological characteristics considerably vary. In this context, matching strips can be directly regarded as the matching results of these ROIs without similarity searching.

Different indices were applied to quantitatively evaluate the matching accuracy of the registered curves and the specific position of ROIs. For the curves, the first measure simply counted the number of cases that the curves exactly passed through the ROI centers (abbreviated as NPL). In this paper, the cases were considered to be NPL as long as the absolute error (AE) was less than 0.35mm between the curves and the ROI centers. The second measure was MAE, which was a widely accepted standard for measuring matching accuracy as described in the Introduction section. All the distance mentioned in this paper referred to the Euclidean distance. We also calculated confidence intervals for different detection sensitivities to determine the appropriate size of the matching strips. Detection sensitivity is regarded as the probability that all ROIs can be detected on second image. A high detection sensitivity corresponded to a large search area around the curves. The area was considered to be the confidence interval in this paper, which indicated the possible location of the ROI centers.

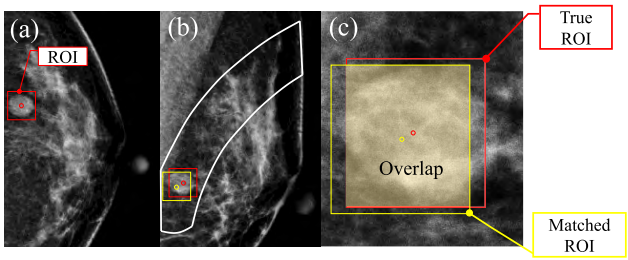

FIGURE 8. (a) CC image with a ROI. (b) Matched results of the ROI on MLO image. (c) Magnification of the overlap between the matched and the reference.

For the accuracy of specific positions, the mean distance between the true ROI centers and matched ROI centers was applied. In addition, the percentages of cases that overlap is greater than 50% and greater than 75% were evaluated. Overlap was defined as the overlapped area between the reference and matched ROI on the MLO images [37], [38], as shown in Fig. 8 (b) and (c).

III. RESULTS

A. RESULTS OF GEOMETRIC MODEL

The three following methods were compared to demonstrate the accuracy of the curves by GM-SS. GM is the geometric model method proposed by Kita *et al.* [20]. The second and the third are Arc and Line method, which have been described in Introduction section. Fig. 9 (a) shows the ROI center of P_l^C on the CC image, l_1 and l_2 represent the radial and horizontal lengths between the center and the nipple, respectively.

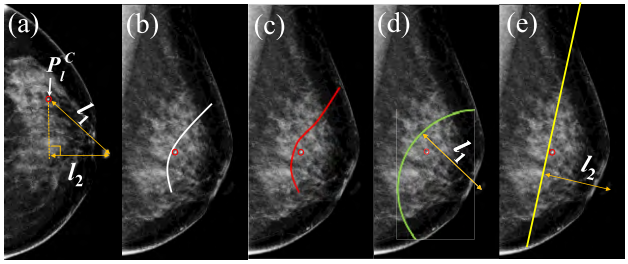

FIGURE 9. Registration results of four different methods. (a) A ROI center P_I^C on the CC image. (b) - (e) Registration results of GM-SS, GM, Arc, and Line, respectively.

Fig. 9 (b) - (e) displays the registration results of GM-SS, GM, Arc, and Line, respectively.

TABLE 2. Registration results of four different methods.

	Objective indices		Detection sensitivity		
	NPL	MAE	80% (320/400)	90% (360/400)	95% (380/400)
GM-MS	45	3.36± 2.90mm	±5.53mm	±7.83mm	±8.77mm
GM	34	5.27± 4.42mm	±8.06mm	±11.68mm	±14.18mm
Arc	28	5.48± 4.59mm	±8.48mm	±12.03mm	±14.44mm
Line	26	5.83± 4.83mm	±9.45mm	±12.26mm	±16.28mm

Results of NPL and MAE for 400 calcifications are listed in the left column of TABLE 2. GM-SS method has the maximum of NPL and the minimum of MAE compared with GM, Arc, and Line. In addition, the smallest standard deviation of ±2.90mm indicates that the curves calculated by GM-SS method are closer to the center of true ROIs in a steady manner. The confidence intervals for different detection sensitivities are listed in the right column of TABLE 2. For detection sensitivities of 80%, 90%, and 95%, the confidence intervals of GM-SS are always smaller than the other methods. For detection sensitivity of 95%, the confidence interval of GM-SS is ±8.77mm, which is considered the size of matching strips for similarity searching. In clinical application, the size can be enlarged suitably to obtain a high recall rate.

Distribution of AE for 400 calcifications is shown in box-plot in Fig. 10. No obvious difference in the median is found among the four methods with the value of 3-4mm. However, the range of AE is from 0 to 15mm for GM-SS and from 0 to 25mm for other methods. There are many cases in GM, Arc and Line method with AE greater than 15mm. In contrast, more than 75% calcifications with AE smaller than 5mm using GM-SS.

The above results were based on the assumption that the known ROI was located on CC image and its corresponding curve was calculated on MLO image. To verify the

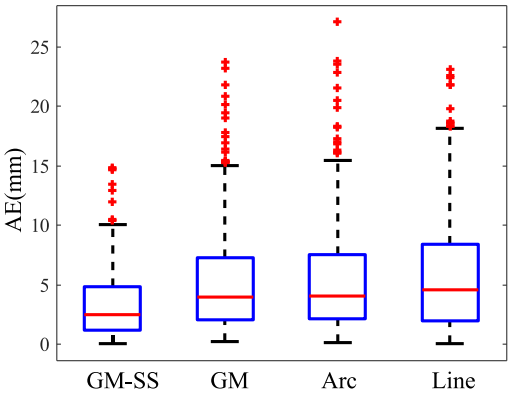

FIGURE 10. Box-plot of AE of four different registration methods.

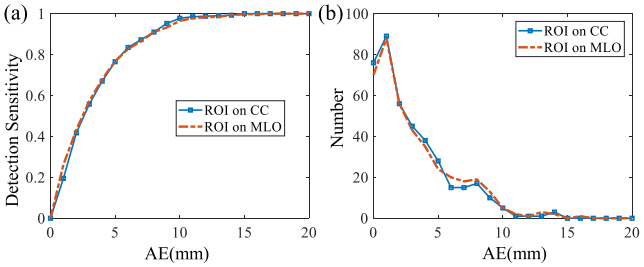

FIGURE 11. AE distribution between the known ROI located on CC image and MLO image, respectively.

TABLE 3. Mean distance (mm) of different ROI sizes for matching calcifications.

ROI size (mm^2)	0.70^2	1.40^2	2.10^2	2.80^2	3.50^2	4.20^2	4.90^2
ISM	4.78± 5.23	3.92± 4.61	4.06± 4.42	5.10± 6.24	8.79± 8.51	11.07± 14.82	12.88± 14.26
SD	11.09± 10.87	8.68± 7.99	6.41± 5.73	8.38± 8.70	10.53± 9.12	11.42± 15.26	15.05± 15.37
IE	5.93± 6.23	7.27± 7.02	4.77± 5.30	6.16± 7.56	9.34± 9.56	11.67± 16.75	14.77± 15.69
CO	8.51± 8.32	6.66± 7.64	5.35± 5.61	7.27± 7.68	10.15± 10.21	11.26± 15.60	12.87± 13.24
PC	7.60± 7.63	5.78± 6.37	5.52± 5.89	7.54± 8.16	9.02± 9.37	12.22± 18.56	13.47± 13.20
MI	8.22± 8.11	7.08± 6.69	5.88± 6.01	9.64± 10.26	11.37± 10.59	13.24± 16.91	14.30± 14.94

reversibility of GM-SS, the curve on CC image was calculated simultaneously assuming the known ROI was located on MLO image. Fig. 11 displays the AE distribution between the known ROI located on CC image and MLO image, respectively. The distribution of AE is demonstrated by detection sensitivity and the number of cases. Results show that similar AE distribution for detection sensitivity and the number of cases, indicating that GM-SS exhibits reversibility well.

B. RESULTS OF SIMILARITY SEARCHING

1) RESULTS OF CALCIFICATION MATCHING

State-of-the-art similarity measures such as standard deviation (*SD*), information entropy (*IE*) [39], Person's correlation (*PC*) [37], [38], *MI* [33], and Cosine measure (*CO*) [40] were

compared to verify the effectiveness of the proposed similarity measure. For randomization, 200 calcification centers were selected as the known ROI centers from the CC images, and the other 200 calcification centers were selected from the MLO images. Seven experiments were performed for comparison to study the effect of ROI sizes on the matching accuracy of calcifications. Size selection was based on the size distribution of calcifications in our datasets. The matching results of the mean distance of the six similarity measures are presented in TABLE 3.

ISM can achieve minimum distance of 3.92±4.61mm with the ROI size of 1.40mm × 1.40mm. Furthermore, for all similarity measures, the mean distances are relatively small when the ROI sizes are approximately equal to the average size of the calcifications.

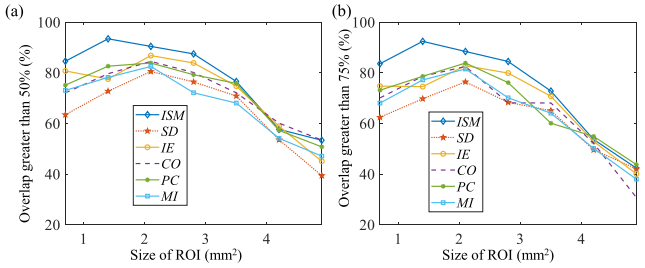

FIGURE 12. Percentages of calcification cases with overlap greater than (a) 50% and (b) 75%.

Similar conclusions can be derived from the percentages of the calcification cases with overlap greater than 50% and 75%, as shown in Fig. 12. *ISM* could realize 93.46% cases with overlap greater than 50% when the ROI size is 1.40mm × 1.40mm. The percentages decrease slightly when the overlap is greater than 75%. The best matching accuracy is 92.46% in cases with overlap greater than 75% using *ISM*. In addition, the matching accuracy is poor when the ROI size is greater than 4.20mm for all similarity measures.

Fig. 13 demonstrates the detection sensitivity of calcifications for different number of candidate ROIs on second-view images. For each similarity measure, the optimal size of ROIs was applied. In this experiment, candidate ROIs were sorted in descending order based on *ISM* value of each ROI. Then detection sensitivities of different similarity measures were evaluated when the number of candidate ROIs was i (i = 1, 2, . . . , 7). Fig.13 shows that the detection sensitivity of ISM is significantly higher than that of other similarity measures, especially when the number of 1-4. Although the detection sensitivities of other similarity measures are increased when the number is 6 and 7, the detection sensitivity of *ISM* is always the highest. In addition, detection sensitivities of all similarity measures tend to be stable when the number of candidate ROIs is 7. The maximum detection sensitivity is no more than 95%, which is in correspondence with the detection sensitivity of 95% for matching strips.

2) RESULTS OF MASS MATCHING

Experiments on different sizes of ROIs were also conducted for masses. Sizes were selected from 11.27mm × 11.27mm

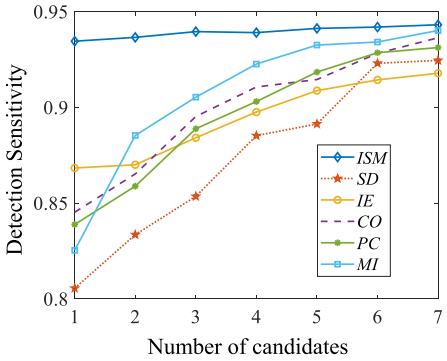

FIGURE 13. Detection sensitivity of calcifications for different numbers of candidate ROIs on second-view images.

to 25.27mm × 25.27mm, based on the size distribution of masses in our datasets. The matching results of the mean distance of the six similarity measures are presented in Table 4. In general, the mean distance of *ISM* is smaller especially when the size of ROIs is between 12.67 mm × 12.67mm and 18.97mm × 18.97mm. The minimum mean distance of *ISM* is 6.15±7.08mm, with the ROI size of 14.07mm × 14.07mm. Except for *SD*, the mean distances of *IE*, *CO*, *PC*, and *MI* are similar. The mean distances are relatively small when the ROI sizes are approximately equal to the average size of the masses for all similarity measures.

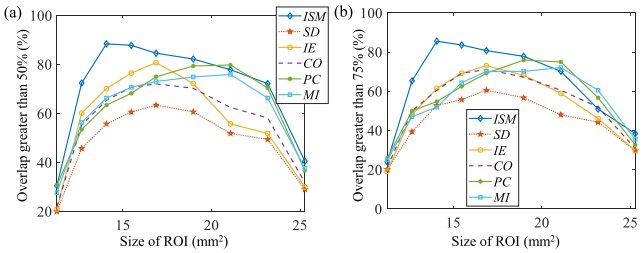

FIGURE 14. Percentages of mass cases with overlap greater than (a) 50% and (b) 75%.

Fig. 14 displays the percentages of cases with overlap greater than 50% and 75%, respectively. Compared with the calcifications, the percentages of the masses are slightly lower because they may change greatly in shape under CC and MLO view compression. *ISM* can realize 88.46% cases with overlap greater than 50% and 85.58% cases with overlap greater than 75%. The matching accuracy is very poor when the ROI sizes are 11.27mm × 11.27mm and 25.27mm × 25.27mm. One possible reason is that too small ROI size can over-magnify a local feature within it, whereas too large ROI size can weaken the features of suspicious lesions. A general rule is that the matching accuracy is relatively high when the size of ROI is approximately equal to the size of suspicious lesions.

The detection sensitivity of masses for different number of candidate ROIs is demonstrated in Fig. 15. For all of the similarity measures, the detection sensitivity can reach more than 85% with increasing number of candidate ROIs.

TABLE 4. Mean distance (mm) of different ROI sizes for matching masses.

ROI size (mm^2)	11.27^2	12.67^2	14.07^2	15.47^2	16.87^2	18.97^2	21.07^2	23.17^2	25.27^2
ISM	16.67 ±13.34	9.74 ±8.14	6.15 ±7.08	7.62 ±8.98	7.80 ±9.55	8.68 ±8.26	9.35 ±9.05	9.53 ±9.79	15.34 ±12.44
SD	18.99 ±16.92	13.53 ±11.23	12.48 ±9.46	10.73 ±9.24	9.23 ±10.33	10.34 ±11.31	12.10 ±10.40	12.34 ±10.55	16.79 ±16.22
IE	18.16 ±15.08	11.42 ±9.59	9.07 ±11.83	8.79 ±12.36	8.64 ±12.89	9.37 ±10.15	11.84 ±13.94	12.45 ±10.76	16.16 ±14.08
CO	16.22 ±14.90	11.86 ±10.12	9.72 ±10.06	9.42 ±8.36	9.50 ±8.87	10.06 ±10.56	10.27 ±11.19	11.91 ±10.53	16.22 ±14.90
PC	16.46 ±17.62	11.89 ±10.47	9.98 ±9.18	9.68 ±14.94	9.58 ±13.24	9.43 ±13.14	9.24 ±13.51	9.48 ±9.69	15.46 ±17.62
MI	16.68 ±14.05	11.67 ±9.09	9.67 ±8.75	9.93 ±12.51	9.03 ±10.93	9.96 ±11.45	9.76 ±10.99	9.86 ±9.92	15.68 ±14.05

TABLE 5. Comparison of results with related works.

Work	Mass	Calcification	Mean distance	Accuracy (75% overlap)	Time consumed
GM-CC	✓	-	8.85mm	79.26%	2-3s
BDT	-	✓	5.78mm	87.78%	7-8s
LDA	✓	✓	7.74mm	81.73%	1-2s
GM-SS	✓	✓	Calcification: 3.92 mm Mass: 6.15 mm	Calcification: 92.46% Mass: 85.58%	2-3s

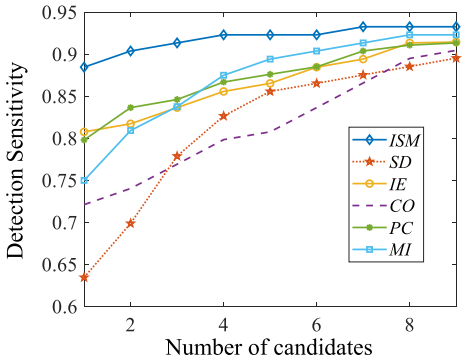

FIGURE 15. Detection sensitivity of masses for different numbers of candidate ROIs on second-view images.

For *ISM*, the optimal detection sensitivity is more than 93% when the number of candidate ROIs is up to seven.

C. RESULT COMPARISONS WITH RELATED WORKS

Results of above two parts show that GM-SS has higher accuracy than commonly used methods in geometric model, and similarity searching. However, to illustrate the effectiveness of GM-SS, the ultimate correspondence results still need to be compared with related works, as shown in Table 5. Specifically, Wei *et al.* [10] proposed a method to link mass correspondence between CC and MLO view images by integrating geometric model (i.e. linear matching strip) and cross correlation (GM-CC for short). In addition, BDT and LDA, which have been already described in Section I, were also compared. Results show that only LDA and GM-SS can correlate both mass and calcification at the same time. GM-CC and BDT can only perform one of the associating tasks, either of mass or of calcification. In addition, this comparisons validate GM-SS has smaller mean distance of 3.92mm for calcification and 6.15mm for mass, and higher accuracy of 92.46% for calcification and 85.58% for mass. Although the time consumption of GM-SS is not the lowest among the four methods, 2-3s is also an acceptable time clinically. Based on the above analysis, GM-SS is a quite attractive correlation method, especially in terms of accuracy.

IV. DISCUSSION

In this work, we have presented an efficient method for matching corresponding ROIs on two-view mammograms by integrating geometric model and image similarity searching. Specifically, by simulating the compression and decompression processes of breast imaging, we established a geometric model to predict the possible location of the ROI center in the second image. Compared with traditional geometric methods, such as Line and Arc method, GM-SS pays more attention to the constraint of 3D information of breast on ROI position. At the same time, compared with the classical 3D methods (i.e. GM method mentioned in this paper), GM-SS is more detailed in simulation process, such as some preprocessing operations in 3D breast restoration, as well as the different compression operations according to different P_c' positions. Modeling of decompression and compression is mainly based on previous experimental results [20]. Precise geometric model helps us to reduce the searching area before matching ROIs without any image information. Smaller searching areas have a significant impact on reducing

false positives, especially for mammogram of dense breasts. In addition, compared with mismatched ROIs, high similarity is shown between same ROIs on CC and MLO images. The experimental results show that *ISM* can work better than five other similarity measures. The main reason is that *ISM* integrates the gray mean and *NMI* of ROI. Gray mean constrains the average of gray values of all pixels in ROI, and *NMI* constrains the probability of gray values of individual pixel in ROI. The experimental results show that the performance of the combination of the two methods is better than that of the conventional similarity measurement.

Our work mainly concentrated on three parts: (i) presenting a curve accurately to register the possible position on second-view mammogram, (ii) providing a method for establishing matching strips, and (iii) proposing a novel integrated similarity measure for matching specific positions of ROIs. The first part is used to calculate curves by constructing a geometric model. First, a free breast can be restored in 3D space from breast contours. Preprocessing operations are applied on MLO contour to acquire two orthogonal projections; such operations include contour extraction, chest line detection, and MLO contour rotation and extension. Three feature points will be selected to present the position of the ROI center in 3D space when the breast is free. This step can be termed as decompression. For the geometric model, the view transformation between CC and MLO can be achieved by changing the coordinates of the breast. Considering that the breast is imaged under pressure in practice, compression will be implemented upon the rotated breast. Three points are mapped onto the MLO image according to the X-ray projection principle. However, the actual path should be a continuous curve. In this context, a simple quadratic interpolation through the three feature points can be presented. A matching strip will be created by confidence interval. Finally, the corresponding ROI can be located on the MLO image through searching in strips by *ISM*. It is worth noting that the matching strips refer to the possible locations of the ROI centers. The area near the matching strips may also be the part of ROIs.

273 pairs of mammograms, including 400 calcifications, and 284 pairs of mammograms with 300 masses were set up to verify the accuracy of curves and specific positions of ROIs, respectively. In actual diagnosis, ROIs may be architectural distortion or asymmetries. However, for architectural distortion and asymmetries, the characteristics on images are not significant and the morphological characteristics considerably vary. In this context, the matching strips can be directly regarded as the matching results of these ROIs without similarity searching. To verify the accuracy of curves, 400 calcifications were applied. The reason for using calcifications is that the edges of calcifications are sharp and the center can be located precisely. In this way, the absolute distance from the ROI center to curves can be easily measured. For GM-SS method, the curves of 45 cases exactly passed through the corresponding centers of ROI (AE $<$ 0.35mm). The MAE was 3.36$\pm$2.90mm for GM-SS, which was much smaller than GM, Arc and Line method. For detection sensitivity of 95%, the confidence interval was $\pm$8.77mm, which was considered to be the size of matching strips for similarity searching. In clinical application, the size of the matching strips can be slightly enlarged to obtain a high recall rate. In addition, GM-MS exhibits reversibility well as shown in Fig. 11. Both of the mammograms with calcifications and masses were evaluated to verify the matching accuracy of the specific position of ROIs. For calcifications, GM-SS can achieve the mean distance of 3.92$\pm$4.61 mm with the ROI size of 1.40mm $\times$ 1.40mm. About 93.46% cases have overlap greater than 50%, and 92.46% of cases have overlap greater than 75%. Compared with calcifications, the matching accuracy of the masses slightly decreases because some of them may change greatly in shape under CC and MLO view compression. Nevertheless, GM-MS can realize 88.46% cases with overlap greater than 50% and 85.58% cases with overlap greater than 75%. In addition, the matching accuracies for calcifications and masses were greatly influenced by the selected size of ROIs. A general rule should be followed when selecting ROIs that the matching accuracy is relatively high when the size of ROI is approximately equal to the size of suspicious lesions. Meanwhile, *ISM* works well for the task of matching corresponding ROIs on two-view images compared with other similarity features. Although in the literature [37], *PC* can provide significantly higher accuracy among 12 similarity characteristics. However, in our experiments, the correlation effect of *PC* was unsatisfactory. The main reason is that the matching tasks are different. In [37], masses on temporal serial mammograms were matched. These mammograms were acquired in the same view but at different times. However, the ROIs of two-view mammograms taken in different views were the targets in our study. The detection task of the latter is more difficult because the breast shape greatly varies in different views due to compression.

V. CONCLUSION

Automatically matching the same ROIs on two-view images is valuable for radiologists in breast cancer diagnosis. This paper proposed GM-SS for matching corresponding ROIs on two-view mammograms by integrating a geometric model and image similarity searching. The main contribution of this work can be summarized as follows: 1) compared with some techniques only acquiring a possible path, GM-SS can obtain specific positions of ROIs on second images. Geometric model in our technique helps us to calculate the possible path with a high accuracy. On this basis, GM-SS further creates a matching strip according to confidence interval, within which the specific position of the ROI can be located via image similarity searching; 2) Results showed that GM-SS can achieve a high accuracy. Geometric model helps us to reduce the searching area before matching ROIs without any image information. Smaller searching areas have a significant impact on reducing false positives; 3) GM-SS is capable of matching any kinds of ROIs because it can always obtain

corresponding matching strips of ROIs via the proposed geometric model. Without any image gray or texture information involved in this step, this technique has great advantages for the task of matching the same ROIs on two-view mammograms, especially for mammograms of dense breasts; 4) This technique has high practicability and flexibility. The only thing radiologists need to do is click on one ROI in CC/MLO image. This method will prompt the location of the same ROIs on the other image. The whole process takes only 2-3 seconds (specific time depends on processor performance).

Recent digital breast tomosynthesis is expected to overcome some inherent limitations of mammography clinical performance caused by overlapping of normal and pathological tissues during the standard 2D projections. However, for most primary hospitals, full field digital mammography (FFDM) is still the most commonly used diagnostic tool for breast cancer. Therefore, the assistant diagnosis technology proposed in this paper remains great significance.

VI. ACKNOWLEDGMENT

(Xiaoman Duan and Genggeng Qin contributed equally to this work.)

REFERENCES

[1] D. S. M. Buist *et al.*, "Influence of annual interpretive volume on screening mammography performance in the United States," *Radiology*, vol. 259, no. 1, pp. 72–84, 2011.
[2] X. Duan *et al.*, "A multiscale contrast enhancement for mammogram using dynamic unsharp masking in Laplacian pyramid," *IEEE Trans. Radiat. Plasma Med. Sci.*, to be published. doi: 10.1109/TRPMS.2018.2876873.
[3] A. Oliver *et al.*, "A review of automatic mass detection and segmentation in mammographic images," *Med. Image Anal.*, vol. 14, no. 2, pp. 87–110, 2010.
[4] G. Carneiro, J. Nascimento, and A. P. Bradley, "Automated analysis of unregistered multi-view mammograms with deep learning," *IEEE Trans. Med. Imag.*, vol. 36, no. 11, pp. 2355–2365, Nov. 2017.
[5] B. Lauby-Secretan *et al.*, "Breast-cancer screening—Viewpoint of the IARC working group," *New England J. Med.*, vol. 372, no. 24, pp. 2353–2358, 2015.
[6] B. Sahiner *et al.*, "Joint two-view information for computerized detection of microcalcifications on mammograms," *Med. Phys.*, vol. 33, no. 7, pp. 2574–2585, 2006.
[7] S. Paquerault, N. Petrick, H. P. Chan, B. Sahiner, and M. A. Helvie, "Improvement of computerized mass detection on mammograms: Fusion of two-view information," *Med. Phys.*, vol. 29, no. 2, pp. 238–247, 2002.
[8] J. Pu, B. Zheng, J. K. Leader, and D. Gur, "An ellipse-fitting based method for efficient registration of breast masses on two mammographic views," *Med. Phys.*, vol. 35, no. 2, pp. 487–494, 2008.
[9] B. Zheng *et al.*, "Multiview-based computer-aided detection scheme for breast masses," *Med. Phys.*, vol. 33, no. 9, pp. 3135–3143, Sep. 2006.
[10] J. Wei *et al.*, "Computer-aided detection of breast masses on mammograms: Dual system approach with two-view analysis," *Med. Phys.*, vol. 36, no. 10, pp. 4451–4460, 2009.
[11] C. Tanner, G. van Schie, J. M. Lesniak, N. Karssemeijer, and G. Székely, "Improved location features for linkage of regions across ipsilateral mammograms," *Med. Image Anal.*, vol. 17, no. 8, pp. 1265–1272, 2013.
[12] M. Velikova, M. Samulski, P. J. F. Lucas, and N. Karssemeijer, "Improved mammographic CAD performance using multi-view information: A Bayesian network framework," *Phys. Med. Biol.*, vol. 54, no. 5, p. 1131, 2009.
[13] M. Altrichter, Z. Ludányi, and G. Horváth, "Joint analysis of multiple mammographic views in CAD systems for breast cancer detection," in *Image Analysis*. Berlin, Germany: Springer, 2005, pp. 760–769.
[14] W. Qian, D. Song, M. Lei, R. Sankar, and E. Eikman, "Computer-aided mass detection based on ipsilateral multiview mammograms," *Acad. Radiol.*, vol. 14, no. 5, pp. 530–538, 2007.
[15] Z. Wang, Q. Qu, G. Yu, and Y. Kang, "Breast tumor detection in double views mammography based on extreme learning machine," *Neural Comput. Appl.*, vol. 27, no. 1, pp. 227–240, 2016.
[16] G. van Schie *et al.*, "Correlating locations in ipsilateral breast tomosynthesis views using an analytical hemispherical compression model," *Phys. Med. Biol.*, vol. 56, no. 15, pp. 4715–4730, 2011.
[17] S. Sanjay-Gopal, H.-P. Chan, T. Wilson, M. Helvie, N. Petrick, and B. Sahiner, "A regional registration technique for automated interval change analysis of breast lesions on mammograms," *Med. Phys.*, vol. 26, no. 12, pp. 2669–2679, 1999.
[18] Y. Yuan, M. L. Giger, H. Li, and C. Sennett, "Correlative feature analysis on FFDM," *Med. Phys.*, vol. 35, no. 12, pp. 5490–5500, 2008.
[19] M. Samulski and N. Karssemeijer, "Optimizing case-based detection performance in a multiview CAD system for mammography," *IEEE Trans. Med. Imag.*, vol. 30, no. 4, pp. 1001–1009, Apr. 2011.
[20] Y. Kita, E. Tohno, R. P. Highnam, and M. Brady, "A CAD system for the 3D location of lesions in mammograms," *Med. Image Anal.*, vol. 6, no. 3, pp. 267–273, 2002.
[21] Y. Kita, R. Highnam, and M. Brady, "Correspondence between different view breast X rays using curved epipolar lines," *Comput. Vis. Image Understand.*, vol. 83, no. 1, pp. 38–56, 2001.
[22] M. Yam, M. Brady, R. Highnam, C. Behrenbruch, R. English, and Y. Kita, "Three-dimensional reconstruction of microcalcification clusters from two mammographic views," *IEEE Trans. Med. Imag.*, vol. 20, no. 6, pp. 479–489, Jun. 2001.
[23] P. Pathmanathan, D. J. Gavaghan, J. P. Whiteley, S. J. Chapman, and J. M. Brady, "Predicting tumor location by modeling the deformation of the breast," *IEEE Trans. Biomed. Eng.*, vol. 55, no. 10, pp. 2471–2480, Oct. 2008.
[24] Y.-H. Chang *et al.*, "Integrated density of a lesion: A quantitative, mammographically derived, invariable measure," *Med. Phys.*, vol. 30, no. 7, pp. 1805–1811, 2003.
[25] G. D. Tourassi, B. Harrawood, S. Singh, J. Y. Lo, and C. E. Floyd, "Evaluation of information-theoretic similarity measures for content-based retrieval and detection of masses in mammograms," *Med. Phys.*, vol. 34, no. 1, pp. 140–150, 2007.
[26] X. Sun, W. Qian, and D. Song, "Ipsilateral-mammogram computer-aided detection of breast cancer," *Comput. Med. Imag. Graph.*, vol. 28, no. 3, pp. 151–158, 2004.
[27] S. C. Yang *et al.*, "3D localization of clustered microcalcifications using cranio-caudal and medio-lateral oblique views," *Comput. Med. Imag. Graph.*, vol. 29, no. 7, pp. 521–532, 2005.
[28] Q. Wang and R. K. Tan, "Fast image/video contrast enhancement based on weighted thresholded histogram equalization," *IEEE Trans. Consum. Electron.*, vol. 53, no. 2, pp. 757–764, May 2007.
[29] S. van Engeland, N. Karssemeijer, and S. N. Timp, "Finding corresponding regions of interest in mediolateral oblique and craniocaudal mammographic views," *Med. Phys.*, vol. 33, no. 9, pp. 3203–3212, 2006.
[30] S. M. Kwok, R. Chandrasekhar, Y. Attikiouzel, and M. T. Rickard, "Automatic pectoral muscle segmentation on mediolateral oblique view mammograms," *IEEE Trans. Med. Imag.*, vol. 23, no. 9, pp. 1129–1140, Sep. 2004.
[31] Y. Li, H. Chen, Y. Yang, and N. Yang, "Pectoral muscle segmentation in mammograms based on homogenous texture and intensity deviation," *Pattern Recognit.*, vol. 46, no. 3, pp. 681–691, 2013.
[32] M. Kallenberg *et al.*, "Unsupervised deep learning applied to breast density segmentation and mammographic risk scoring," *IEEE Trans. Med. Imag.*, vol. 35, no. 5, pp. 1322–1331, May 2016.
[33] J. P. W. Pluim, J. B. A. Maintz, and M. A. Viergever, "Mutual-information-based registration of medical images: A survey," *IEEE Trans. Med. Imag.*, vol. 22, no. 8, pp. 986–1004, Aug. 2003.
[34] J. J. Moré, "The Levenberg–Marquardt algorithm: Implementation and theory," in *Numerical Analysis*. Berlin, Germany: Springer, 1978, pp. 105–116.
[35] E. A. Sickles, C. J. D'Orsi, L. W. Bassett, C. M. Appleton, W. A. Berg, and E. S. Burnside, "ACR BI-RADS Mammography," in *ACR BI-RADS, Breast Imaging Reporting and Data System*, 5th ed. Reston, VA, USA: American College of Radiology, 2013.
[36] M. Raghu *et al.*, "Tomosynthesis in the diagnostic setting: Changing rates of BI-RADS final assessment over time," *Radiology*, vol. 281, no. 1, pp. 54–61, 2016.
[37] P. Filev, L. Hadjiiski, B. Sahiner, H. P. Chan, and M. A. Helvie, "Comparison of similarity measures for the task of template matching of masses on serial mammograms," *Med. Phys.*, vol. 32, no. 2, pp. 515–529, 2005.

[38] L. Hadjiiski, H.-P. Chan, B. Sahiner, N. Petrick, and M. A. Helvie, "Automated registration of breast lesions in temporal pairs of mammograms for interval change analysis—Local affine transformation for improved localization," *Med. Phys.*, vol. 28, no. 6, pp. 1070–1079, 2001.
[39] D.-Y. Tsai, Y. Lee, and E. Matsuyama, "Information entropy measure for evaluation of image quality," *J. Digit. Imag.*, vol. 21, no. 3, pp. 338–347, 2008.
[40] B. M. Sarwar, G. Karypis, J. A. Konstan, and J. Riedl, "Item-based collaborative filtering recommendation algorithms," in *Proc. Int. Conf. World Wide Web*, 2001, pp. 285–295.

XIAOMAN DUAN received the B.E. degree from Southern Medical University, in 2017, where she is currently pursuing the master's degree with the School of Biomedical Engineering. Her research interests include X-ray imaging and geometric calibration of cone-beam CT.

GENGGENG QIN received the bachelor's degree in medicine from Sun Yat-sen University, Guangzhou, China, and the master's degree in medicine from Southern Medical University, Guangzhou, China. He is currently an Associate Chief Physician with the Department of Radiology, Nanfang Hospital, Southern Medical University. He is also a Visiting Scholar with the Department of Radiation Oncology, University of Texas Southwestern Medical Center, Dallas, TX, USA. He has published 26 journal papers. His current research interests include radiomics, medical image analysis, deep learning, machine learning, and artificial intelligence.

QINGQING LING received the B.E. degree from Southern Medical University, in 2017, where she is currently pursuing the master's degree with the School of Biomedical Engineering. Her research interests include X-ray imaging and image-guided radiation therapy.

SINA WANG received the bachelor's degree in medical imaging from China Medical University, in 2016. She is currently pursuing the master's degree in medical imaging with Southern Medical University. Her research interests include breast disease detection and diagnostic imaging.

ZEYUAN XU received the bachelor's degree in medical imaging from Southern Medical University, in 2016, where she is currently pursuing the master's degree with the School of Imaging Medicine and Nuclear Medicine. Her research interest includes mammography in the diagnosis of the breast cancer.

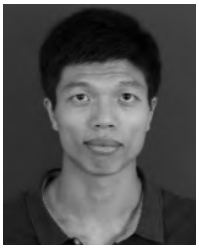

HUI ZENG graduated in medical imaging from Southern Medical University, in 2013. He is currently pursuing the master's degree in imaging medicine and nuclear medicine with Southern Medical University. He was a Doctor with the Department of Radiology, Nanfang Hospital, Southern Medical University. His current research interests include the screening and diagnosis of early breast cancer and artificial intelligence of breast imaging.

BIN LI received the B.E. degree from the National University of Defense Technology, the master's degree from Information Engineering University, and the Ph.D. degree in biomedical engineering from Southern Medical University. He is currently a Professor with the Department of Mathematical Physics, School of Biomedical Engineering, Southern Medical University. His research interests include medical image processing and pattern recognition.

WEIGUO CHEN graduated from the Department of Clinical Medicine, First Military Medical University, in 1984, and received the master's degree in imaging medicine and nuclear medicine from Sun Yat-sen Medical University. He is currently a Chief Physician, Professor, and the Director of the Radiology Department, Nanfang Hospital, Southern Medical University. His main research interests include multimodal imaging diagnosis of breast diseases, and research and development of digital breast equipment and clinical application.

LINGHONG ZHOU received the B.E. degree from the Hefei University of Technology and the master's degree from Tsinghua University. He is currently a Professor with the School of Biomedical Engineering, Institute of Medical Instrument, Southern Medical University, the Executive Director of the Medical Physics Division, Tumor Radiation Branch, Chinese Medical Association, and the Standing Director of the Medical Instrument Branch, China Instrument and Control Society. He received one Second Class Prizes of The State Scientific and Technological Progress Award and seven Ministerial and Provincial-Level Science and Technology Awards. He actively supervises many students at all level of study-bachelor's, master's, and Ph.D. His research interests include Monte Carlo simulation, image-guided radiation therapy, and adaptive radiation therapy.

YUAN XU received the B.E. degree in electronic and information engineering and the Ph.D. degree in biomedical engineering from Southern Medical University, China. He has published a number of research articles in image-guided radiation therapy and CBCT imaging. He is currently an Associate Professor with the School of Biomedical Engineering, Southern Medical University. His research interests include Monte Carlo simulation, X-ray imaging, and image-guided radiation therapy.